

# Probing Adsorption Behaviors of BSA onto Chiral Surfaces of Nanoparticles

Xinyi Wang, Xiaofeng Wang, Mingzhe Wang, Di Zhang, Qi Yang, Tao Liu, Rong Lei, Shuifang Zhu, Yuliang Zhao, and Chunying Chen\*

Chiral properties of nanoscale materials are of importance as they dominate interactions with proteins in physiological environments; however, they have rarely been investigated. In this study, a systematic investigation is conducted for the adsorption behaviors of bovine serum albumin (BSA) onto the chiral surfaces of gold nanoparticles (AuNPs), involving multiple techniques and molecular dynamic (MD) simulation. The adsorption of BSA onto both L- and D-chiral surfaces of AuNPs shows discernible differences involving thermodynamics, adsorption orientation, exposed charges, and affinity. As a powerful supplement, MD simulation provides a molecular-level understanding of protein adsorption onto nanochiral surfaces. Salt bridge interaction is proposed as a major driving force at protein–nanochiral interface interaction. The spatial distribution features of functional groups ( $-\text{COO}^-$ ,  $-\text{NH}_3^+$ , and  $-\text{CH}_3$ ) of chiral molecules on the nanosurface play a key role in the formation and location of salt bridges, which determine the BSA adsorption orientation and binding strength to chiral surfaces. Sequentially, BSA corona coated on nanochiral surfaces affects their uptake by cells. The results enhance the understanding of protein corona, which are important for biological effects of nanochirality in living organisms.

## 1. Introduction

Chirality at a nanoscale level<sup>[1]</sup> is a major topic in chemistry and biology due to its unique properties, such as optical activity,<sup>[2]</sup> mechanical strength,<sup>[3]</sup> asymmetric catalysis,<sup>[4]</sup> and electromagnetic properties.<sup>[5]</sup> The rapid growth in nanotechnology has increased the chances of nanomaterials coming into contact with humans and the environment.<sup>[6]</sup> However, exploration of chirality-related biological effects and toxicity of nanomaterials has only begun recently.<sup>[7]</sup> It is a widely accepted fact that the surface of nanoparticles (NPs) immediately adsorbs proteins and forms a so-called “protein corona”<sup>[8]</sup> when NPs enter a biological environment, which determines the biological fate of NPs. Although numerous efforts have been made to investigate the roles of the physicochemical properties of NPs, i.e., chemical composition, size,

shape, surface charge, roughness, hydrophobicity, etc., in the formation of protein corona,<sup>[9]</sup> studies on the influence of nanochirality on protein corona are more worthy to be explored.<sup>[10]</sup> Amino acids, as the basic building blocks of proteins, are L-enantiomers (excluding glycine) by which proteins also show unique enantiomeric forms. Studies have been increasingly focusing on the stereoselective interaction between chiral NPs and biological systems at both the protein level<sup>[11]</sup> and cellular level,<sup>[12]</sup> resulting in chirality-related nanobiological effects.<sup>[13]</sup> Therefore, the understanding of nanochiral recognition at a biomacromolecular level would provide more information to understand the mechanism of the complicated nanobiological effects in biological systems.<sup>[14]</sup>

Nanosized chiral formations show diversity, involving either single objects with intrinsically chiral crystal/chiral configuration<sup>[15]</sup> or the assembly of several subunits into tridimensional chiral structures.<sup>[16]</sup> It is always difficult to determine the differences in protein binding behaviors on different chiral surfaces, because these are sometimes too weak to distinguish.<sup>[13a]</sup> Thus, effective methods to investigate the process and mechanism of nanochiral recognition at the protein level are required. A wide range of characterization techniques have been employed to study the interaction between proteins and nanomaterials including dynamic light scattering (DLS),<sup>[17]</sup> fluorescence correlation spectroscopy,<sup>[18]</sup> small-angle X-ray scattering,<sup>[19]</sup> transmission electron microscopy (TEM),<sup>[20]</sup> atomic force


Dr. X. Wang, M. Wang, T. Liu, Prof. Y. Zhao, Prof. C. Chen  
CAS Key Laboratory for Biomedical Effects  
of Nanomaterials and Nanosafety  
& CAS Center for Excellence in Nanoscience  
National Center for Nanoscience and Technology of China  
University of Chinese Academy of Sciences  
Beijing 100190, China  
E-mail: chenchy@nanoctr.cn

Dr. X. Wang  
College of Environment  
Liaoning University  
Shenyang 110036, China

Dr. X. Wang, D. Zhang, Q. Yang  
College of Science  
Shenyang Agricultural University  
Shenyang 110866, China

Dr. X. Wang  
CAS Key Laboratory for Biomedical Effects of  
Nanomaterials and Nanosafety  
Institute of High Energy Physics  
Chinese Academy of Sciences (CAS)  
Beijing 100049, China

Dr. R. Lei, Prof. S. Zhu  
Institute of Plant Quarantine  
Chinese Academy of Inspection and Quarantine  
Beijing 100029, China

 The ORCID identification number(s) for the author(s) of this article can be found under <https://doi.org/10.1002/sml.201703982>.

DOI: 10.1002/sml.201703982

microscopy,<sup>[21]</sup> isothermal titration calorimetry,<sup>[22]</sup> circular dichroism (CD) spectroscopy,<sup>[23]</sup> and Fourier transform infrared spectroscopy (FTIR).<sup>[24]</sup> These measurement methods allow us to obtain some information about protein adsorption behaviors onto the surface of nanomaterials, including size change, binding strength, thermodynamic, adsorption orientation, and conformational change. These methods and techniques also provide a great reference to explore chiral recognition between proteins and chiral nanomaterials. However, a more detailed characterization of protein–nanomaterial interaction remains a critical technical challenge. Computer simulation has played a key role in understanding the mechanism of interaction between proteins and nanomaterials.<sup>[25]</sup> Overall, it is necessary to develop an integrated strategy involving multiple methods and techniques for understanding the interaction between proteins and nanomaterials.

Bovine serum albumin (BSA) has widely been used as a model protein in research due to its excellent biocompatibility and similarity with human serum albumin.<sup>[26]</sup> Recently, BSA has been designed as the ideal candidate for applications in nanoparticulate and microparticulate drug carrier systems, especially for cancer therapy.<sup>[27]</sup> Understanding the corona behaviors on nanosurface is crucial for enhancing the efficiency of drug encapsulation/delivery to cancer cells. Gold nanoparticles (AuNPs) can serve as an ideal nanomaterial to study the protein–nanochiral interface due to their ease of preparation and surface modification.<sup>[28]</sup> AuNPs have been shown to display a mirror–image relationship at wavelengths between 190 and 260 nm and surface plasmon-circular dichroism (SP-CD) at 520 nm by modification of chiral molecules.<sup>[29]</sup> Thus, we studied the adsorption behaviors of BSA on the chiral surface of AuNPs, using several techniques including DLS, quartz crystal microbalance with dissipation monitoring (QCM-D),

fluorescence, zeta-potential, CD, and attenuated total reflection infrared spectroscopy (ART-IR), to obtain information regarding thermodynamics, layer thickness, adsorption orientation, and conformation change. We also utilized molecular dynamic (MD) simulation to understand the mechanism occurring at the protein–nanochiral interface at a molecular level. This study may provide valuable information to address increasing concerns regarding the biological effects of chiral nanomaterials on organisms.

## 2. Results and Discussion

### 2.1. Preparation of Gold Nanoparticles with Chiral Surfaces

AuNPs were prepared by citrate reduction of  $\text{HAuCl}_4$ <sup>[30]</sup> and the concentration of prepared AuNPs was about  $15 \times 10^{-9} \text{ M}$  ( $180 \mu\text{g mL}^{-1}$ ).<sup>[31]</sup> The particle size as determined by TEM was  $\approx 14 \text{ nm}$  (Figure S1, Supporting Information). Herein, we selected penicillamine (Pen) as the chiral adsorbate to construct the nanochiral surfaces by Au–S chemical bonding interaction (Figure 1a), which were labeled as AuNPs(L) and AuNPs(D). Pen is a simple chiral molecule containing just one chiral center; the nanochiral surface constructed using Pen is relatively simple in structure and favorable to investigate the mechanism of protein adsorption. Characterization using FTIR spectra, plasmon absorption spectra, and CD spectra (Figures S2–S4, Supporting Information) demonstrated the modification of Pen on AuNPs and the formation of chiral surfaces on AuNPs. Bonding density measurements (Figure S5, Supporting Information) showed that the surfaces of AuNPs were almost completely covered by L-Pen or D-Pen molecules. Utilizing MD simulations, the spatial distribution

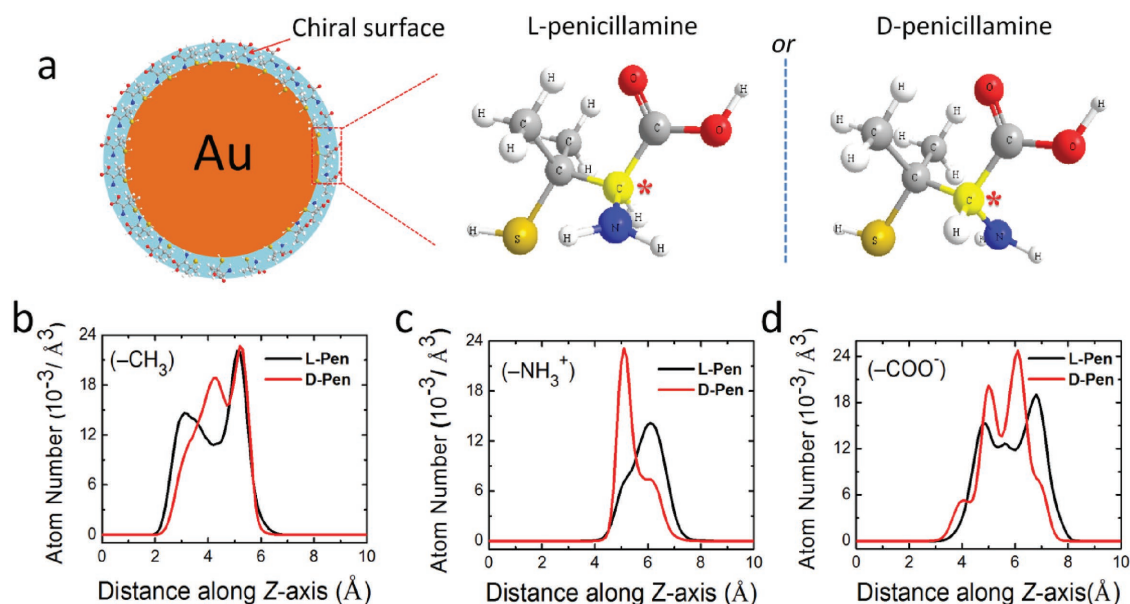


**Figure 1.** Preparation of chiral Pen–AuNPs and morphological features of chiral interfaces. a) Schematic diagram of surface modification of AuNPs with L-Pen or D-Pen molecules. b–d) The spatial distribution of  $-\text{CH}_3$ ,  $-\text{NH}_3^+$ , and  $-\text{COO}^-$  groups on L-chiral/D-chiral surfaces, respectively, by counting the amount of each functional group per unit distance (2 Å) along the Z-axis direction perpendicular to the surface of AuNPs based on MD simulation (20 ns).

of functional groups ( $-\text{COO}^-$ ,  $-\text{NH}_3^+$ , and  $-\text{CH}_3$ ) of Pen around the chiral center was mapped by counting the number of each functional group present per unit distance (2 Å) along the Z-axis direction perpendicular to the nanosurface. The results (Figure 1b) showed that the spatial distribution of functional groups ( $-\text{COO}^-$ ,  $-\text{NH}_3^+$ , and  $-\text{CH}_3$ ) in Pen around the chiral center along Z-axis was different between AuNPs(L) and AuNPs(D).

## 2.2. Binding Thermodynamics of BSA onto Chiral Surfaces of Pen–AuNPs

AuNPs can quench the fluorescence of fluorophores via efficient energy-transfer from the fluorophore to AuNP surfaces over spatial distances as large as 10–20 nm.<sup>[32]</sup> The autofluorescence quenching of proteins by AuNPs could be described by the modified Stern–Volmer equation, by which the effective quenching constant ( $K_a$ ) at different temperatures was estimated (Figure S6, Supporting Information). Sequentially, we could calculate the enthalpy change ( $\Delta H$ ) and entropy change ( $\Delta S$ ) according to the van't Hoff equation, and then derive Gibbs free energy change ( $\Delta G$ ). The experimental details are described in the Experimental Section. All obtained thermodynamic parameters are listed in **Table 1**. The adsorption of BSA onto both chiral surfaces of Pen–AuNPs was found to be a spontaneous and exothermic process based on negative  $\Delta G$ , negative  $\Delta H$ , and positive  $\Delta S$ . Some differences between chiral surfaces were also found. Compared to D-chiral surface, the interaction of BSA with L-chiral surface of AuNPs released more heat and caused greater  $\Delta S$ . Therefore, we next needed to obtain some direct or indirect evidence to support the existence of these differences.

## 2.3. Characterization of BSA Adsorption on Chiral Surfaces of AuNPs

Some available techniques (such as X-ray crystallography, NMR, or dual polarization interferometry) may become more complicated, time-consuming, and challenging when used to treat a hybrid system of protein and nanomaterials. Alternatively, we focused on the changes in the size and surface exposed charge of the NP–protein system as an indirect means of sketching protein morphology. Herein, we employed the DLS technique to determine the changes in the hydrodynamic radius ( $\Delta R_H$ ) of AuNPs before and after interacting with BSA (Figure 2a). Sequentially, the data were fitted using

**Table 1.** Thermodynamic parameters of the interaction between BSA and Pen–AuNPs based on fluorescence quenching data.

Chiral surface	$\Delta H$ [kJ mol <sup>-1</sup> ]	$\Delta S$ [J mol <sup>-1</sup> K <sup>-1</sup> ]	$\Delta G$ [kJ mol <sup>-1</sup> ]
AuNPs(L)	-12.351	137.21	310 K: -50.954
			300 K: -49.582
AuNPs(D)	-8.420	124.61	310 K: -50.978
			300 K: -49.732

Hill equation to obtain the dissociation constant ( $K_D'$ ), Hill coefficient ( $n$ ), protein layer thickness ( $\Delta R_H$ ), and maximum adsorption number ( $N_{\text{max}}$ ). Results (Figure 2b,c) showed the  $\Delta R_H$  of Pen–AuNPs increased upon the addition of BSA until a plateau was reached. The increase in the Pen–AuNP radius ( $\Delta R_H$  values) was 3.3 nm for AuNPs(L) and 3.4 nm for AuNPs(D). The structure of BSA could be approximately considered as an equilateral triangular prism with sides of  $\approx 8$  nm and a height of  $\approx 3$  nm (Figure 1d).<sup>[26]</sup> Thus, we could deduce that BSA formed a monolayer attachment around the AuNPs(L) or AuNPs(D) via its large triangular faces. The complete surface coverage was estimated to be  $\approx 58$  BSA molecules on Pen–AuNPs, based on the surface area of a sphere with the radius ( $R_H(0) + \Delta R_H/2$ ).<sup>[18b]</sup> The  $N_{\text{max}}$  values were  $61 \pm 4$  for AuNPs(L) and  $60 \pm 3$  for AuNPs(D). Thus, the BSA molecules sealed the chiral surfaces of Pen–AuNPs with a dense monolayer. The Hill coefficient ( $n$ , markedly less than one) indicated an anticooperative interaction process. The dissociation coefficient,  $K_D'$  of AuNPs(L)–BSA was almost 1/3–1/2 order of magnitude lower than that of AuNPs(D)–BSA, reflecting a markedly stronger interaction at the L-chiral interface, which was consistent with the results of fluorescence quenching.

Although we determined that BSA attached to AuNPs(L) or AuNPs(D) via its large triangular faces based on  $\Delta R_H$  values, we could not ascertain which triangular face was favorable to contact with Pen–AuNPs based on the  $\Delta R_H$  values alone. Considering the irregular protein surfaces and uneven distribution of surface charges, it was possible to judge the adsorption orientation by calculating the exposed charges after BSA attached to NPs. We marked the two triangular faces of BSA as concave and convex based on their morphology. Figure 2d shows the distribution of charged amino acids on each side face of BSA. The number of charges on each side face of the protein, based on Figure 2d, by calculating a solvent-accessible surface area greater than 50% is shown in Figure 2e. However, the net charges on the concave and convex side faces were almost the same. Obviously, it was unreasonable to determine protein adsorption orientation based on the whole surface potential measurement of the AuNP–Pen–BSA system. As shown in Figure S7 (Supporting Information), the surface zeta potential of AuNPs(L) and AuNPs(D) eventually tended to the potential of pure BSA after forming the BSA corona. Considering the irregular protein morphology and uneven distribution of surface charges, it was possible to determine the protein adsorption orientation by counting the local charges of protein in an upper region when the protein attached to the nanosurface via a specific orientation (Figure 2f). Therefore, the QCM-D technique was used to monitor the interaction between BSA-adsorbed Pen–AuNPs and positively charged supported lipid bilayers (SLBs), as illustrated schematically in Figure 2g. In the above process, only the upper part of the protein was in contact with the SLBs. The results (Figure S8, Supporting Information) indicate SLB formation [1,2-dioleoyl-sn-glycero-3-phosphocholine:1,2-dioleoyl-sn-glycero-3-ethylphosphocholine (DOPC:DOEPC, 8:2)] on the silicon oxide substrate. The value of  $\Delta f$  was used to scale the mass of NPs adsorbed onto the SLBs. The results (Figure 2h) showed that the AuNP(D)–BSA complex had a larger amount of adsorption onto SLBs

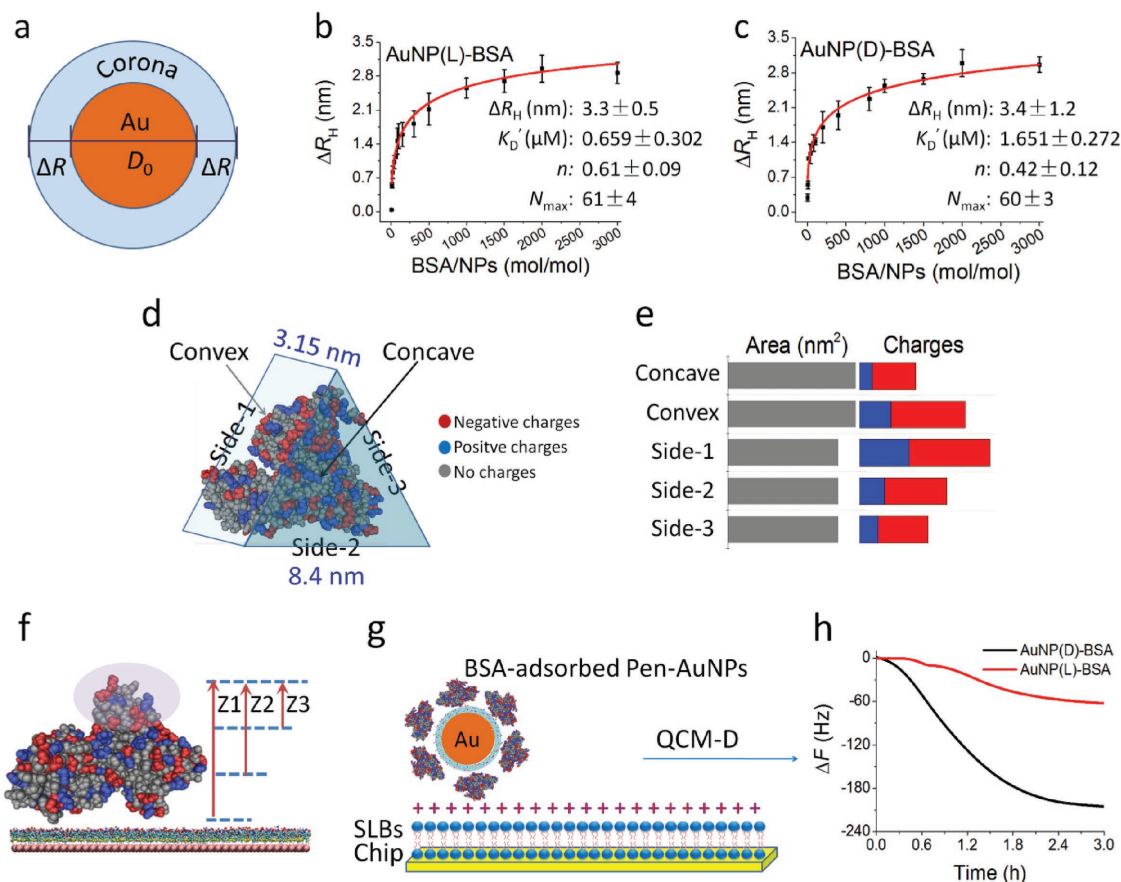


**Figure 2.** Adsorption orientation of BSA on the chiral surfaces of AuNPs. a) Cartoon presentation for the measurement of adsorption thickness of the BSA layer on chiral surfaces of AuNPs by DLS. b,c) The hydrodynamic radius measurements of AuNP(L)-BSA and AuNP(D)-BSA, plotted as a function of the BSA concentration. The final concentrations of all AuNP solutions were fixed at  $150 \mu\text{g mL}^{-1}$ , and DLS measurements were performed after mixing Pen-AuNPs with the desired concentrations of BSA for 1 h at room temperature. The curves (red solid lines) were fitted according to the Hill equation, and the best-fit parameters are listed on the right. d) The distribution of charged amino acids on different side faces of BSA. The 3D structure of BSA was described using a space-filling model (PDB ID: 4F5S) with color-coded charge types (red, negative charge; blue, positive charge; grey, no charge). e) Statistical distribution of charged amino acids on each side of BSA. f) Schematic presentation for the detection of exposed surface charges of adsorbed BSA on Pen-AuNPs. g) Schematic of interaction between AuNP-Pen-BSA and SLBs (DOPC:DOEPC, 8:2) monitored by QCM-D. h) QCM-D results of the adsorption of AuNP-Pen-BSA onto SLBs.

than the AuNP(L)-BSA complex, indicating that AuNP(D)-BSA carried more negative charges than AuNP(L)-BSA at the contact site. It could thus be deduced that BSA adopts different orientations when adsorbing onto AuNPs with different chiral surfaces.

#### 2.4. Determination of BSA Conformation Using Synchrotron Radiation ART-IR

We performed synchrotron radiation ART-IR measurements to analyze the possible influence of chiral surfaces of AuNPs on BSA secondary structures when the protein adsorbed onto Pen-AuNPs with different orientations. IR measurement with a synchrotron radiation beamline has been developed as an effective method to investigate protein secondary structures based on the adsorption bands of amide groups, mainly including amide I ( $\approx 1650 \text{ cm}^{-1}$ ), amide II ( $1550 \text{ cm}^{-1}$ ), and amide III ( $\approx 1300 \text{ cm}^{-1}$ ).<sup>[24]</sup> Especially, the amide I region (involving C=O stretching) has been widely

recognized due to its sensitivity to protein conformation changes. The results (Figure 3a-c) showed band narrowing of the amide I region by both second-derivative (SD) and Fourier self-deconvolution (FSD) analyses. The assignments of amide I band positions to secondary structure are listed in Table S1 (Supporting Information). Percentage distributions of the secondary structures of BSA are listed in Table 2. The results showed that chiral surfaces of AuNPs did not compromise the secondary structures of BSA when they are attached to Pen-AuNPs. Secondary structure is formally defined by the pattern of hydrogen bonds between the amine hydrogen and carbonyl oxygen atoms in the peptide backbone. In addition, it is well known that BSA is a “rigid” protein, in which 17 pairs of disulfide bonds between cysteine residues help maintain the BSA tertiary structure. It could be proposed that BSA binding to chiral surfaces of Pen-AuNPs did not disrupt the BSA conformation. Therefore, it was important to know the forces involved in the protein-nanochiral interface, to obtain a molecule-level understanding of the interaction between the protein and the chiral surfaces of AuNPs.



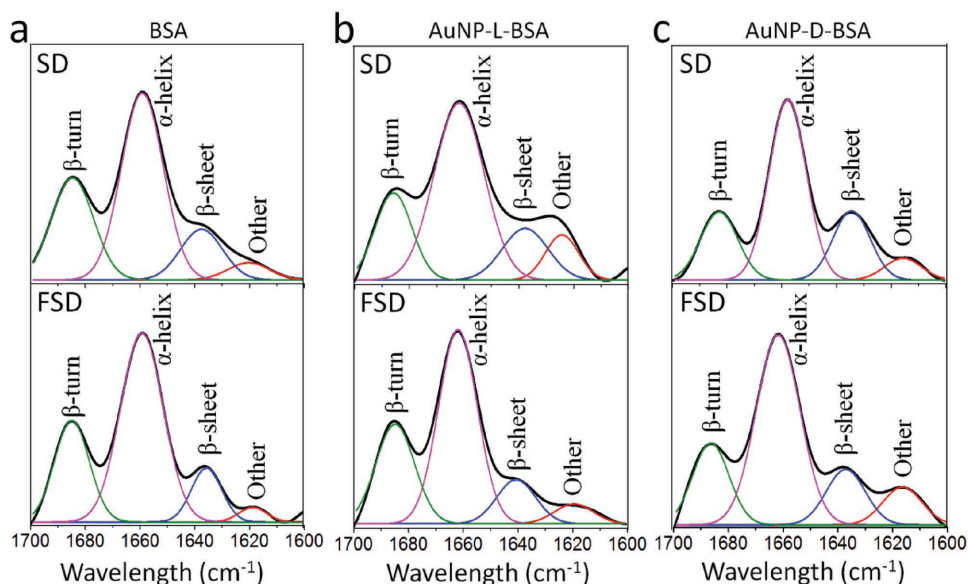


**Figure 3.** ART-IR analysis of secondary structures of BSA adsorbed on the chiral surfaces of AuNPs. a–c) Curve-fitted inverted second-derivative (SD) and curve-fitted inverted Fourier self-deconvolution (FSD) of amide I spectra of BSA adsorbed on chiral surfaces of AuNPs. Curve fitting was carried out using the OMNIC software (<http://www.thermoscientific.com/en/products/fourier-transform-infrared-spectroscopy-ftir.html>).

### 2.5. MD Simulations of the Interaction between BSA and Nanochiral Surfaces

As suggested by the fluorescence quenching and DLS results, BSA adopted different orientations and binding strength when adsorbing onto both chiral surfaces of Pen–AuNPs. To illustrate the observed effects, we performed MD simulations (120 ns) of the interaction between BSA and the nanochiral surfaces. Considering the modification of sulfur-containing molecules occurring primarily on Au{111} surfaces,<sup>[33]</sup> we adopted the flat {111} facets as a simplified model system to investigate the adsorption behaviors of BSA. In our simulation, four systems were to be built, involving both triangular sides of BSA (concave and convex) and two nanochiral surfaces (e.g., AuNPs(L) and AuNPs(D)). The related videos of dynamic interaction are supplied as Videos S1–S4 (Supporting Information). A group of representative snapshots of four sys-

tems from state trajectories at 120 ns is shown (Figure 4a). It was obvious that the contact sites and adsorption orientation of BSA on L-chiral or D-chiral surfaces were different. Notably, the protein conformation did not change during adsorption onto AuNPs, which was consistent with the ART-IR results. Furthermore, we counted the number of contacted amino acids, locally exposed charges, and the height of protein along the time, and mean values were obtained by averaging frames over 100–120 ns to quantify the difference between nanochiral surfaces (Figure 4c–e).

The contact amino acids of BSA within 4.5 Å distance from the chiral surfaces of AuNPs (more than 75% contact ratio) are listed in Table S2 (Supporting Information). The number of contact amino acids reflects the binding strength between the protein and chiral surfaces. Results (Figure 4c) showed that the concave and convex faces of BSA attached to the same chiral surface with the same amount of amino acids, indicating that the concave and convex faces of BSA adsorbed onto Pen–AuNPs with the same probability. However, the amounts of contact amino acids (the mean of concave and convex faces) on different nanochiral surfaces were different. It was obvious that the affinity of BSA attached to L-chiral surface was stronger than that of the D-chiral surface, which was consistent with the  $K_d$  value (Figure 1b). Results (Figure 4d) showed that the exposed positive charges and negative charges (counted in the upper 1/3 region of BSA molecule) were different when BSA contacted different chiral surfaces of AuNPs, indicating different contact sites and adsorption orientation of BSA on L-chiral and D-chiral surfaces. The overall average of exposed negative charges of BSA after adsorbing onto L-chiral surface was less than that for D-chiral surface, which was consistent with the QCM-D results (Figure 2h). Although the final average values of protein height were similar, results (Figure 4e) showed that the specific situations on both chiral surfaces were different,

**Table 2.** Percentage distributions of BSA secondary structures before and after interaction with Pen–AuNPs as determined by ART-IR spectroscopy.

Protein	Methods	Secondary structures [%]			
		$\alpha$ -helix	$\beta$ -sheet	$\beta$ -turn	Others
BSA	X-ray <sup>a)</sup>	74.9	3.1	1.4	20.6
	SD <sup>b)</sup>	54.6 ± 3.0	13.4 ± 1.2	24.9 ± 5.2	7.2 ± 3.4
	FSD <sup>c)</sup>	54.8 ± 2.8	13.9 ± 1.8	25.7 ± 3.7	5.9 ± 2.5
AuNP-D-BSA	SD <sup>b)</sup>	54.2 ± 2.4	18.7 ± 3.0	18.8 ± 3.0	8.4 ± 1.9
	FSD <sup>c)</sup>	54.1 ± 2.7	16.8 ± 3.1	22.9 ± 1.3	6.8 ± 3.5
AuNP-L-BSA	SD <sup>b)</sup>	51.6 ± 2.3	19.5 ± 5.6	16.7 ± 6.6	12.2 ± 2.1
	FSD <sup>c)</sup>	54.1 ± 1.5	15.7 ± 4.9	23.0 ± 6.6	7.3 ± 3.0

<sup>a)</sup>Data from X-ray structure; <sup>b)</sup>Data from second-derivative FTIR analysis; <sup>c)</sup>Data from Fourier self-deconvolution FTIR analysis.

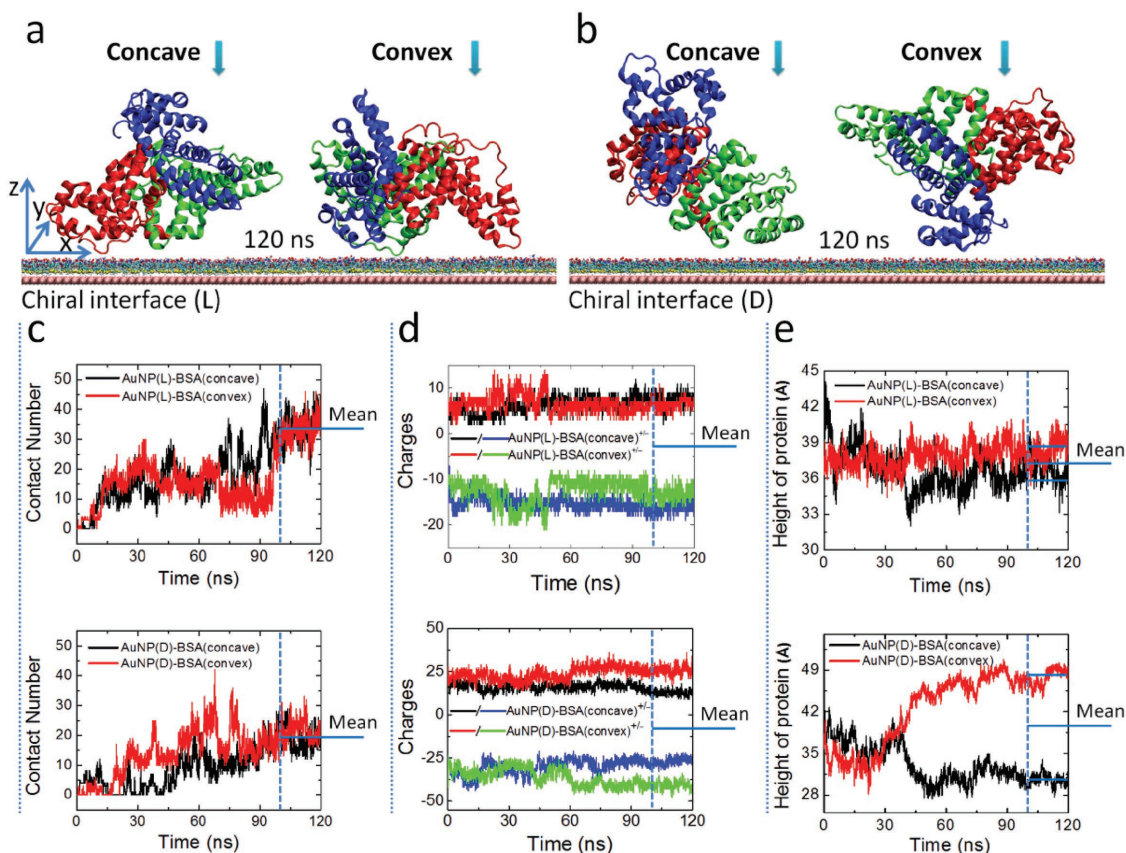


**Figure 4.** MD simulations demonstrating the adsorption behaviors of BSA on the chiral surfaces of AuNPs. a,b) Representative snapshots from state trajectories at 120 ns of four systems involving two triangular sides of BSA (concave and convex) and two chiral (L/D) surfaces of AuNPs. c) The contact number of amino acids on BSA surfaces within 4.5 Å distance of the chiral surfaces of AuNPs. Mean values are obtained by averaging frames over 100–120 ns. The contact number of amino acids on L-surface is 37 and that on D-surface is 19. d) Distribution of exposed surface charges of BSA (only 1/3 of the upper protein is considered). Net charges are averaged over 100–120 ns. The net charge in L-surface is  $-7.5$  eV and that in D-surface is  $-14.5$  eV. e) Height of the protein in the Z-axis direction along with time. Mean protein height on L-surface is  $37.2$  Å and that on D-surface is  $39.4$  Å.

resulting from the difference in contact sites and adsorption orientation. Overall, MD simulation results indicated that BSA attached to the L-chiral or D-chiral surfaces of AuNPs with different contact sites, adsorption orientation, and binding strength.

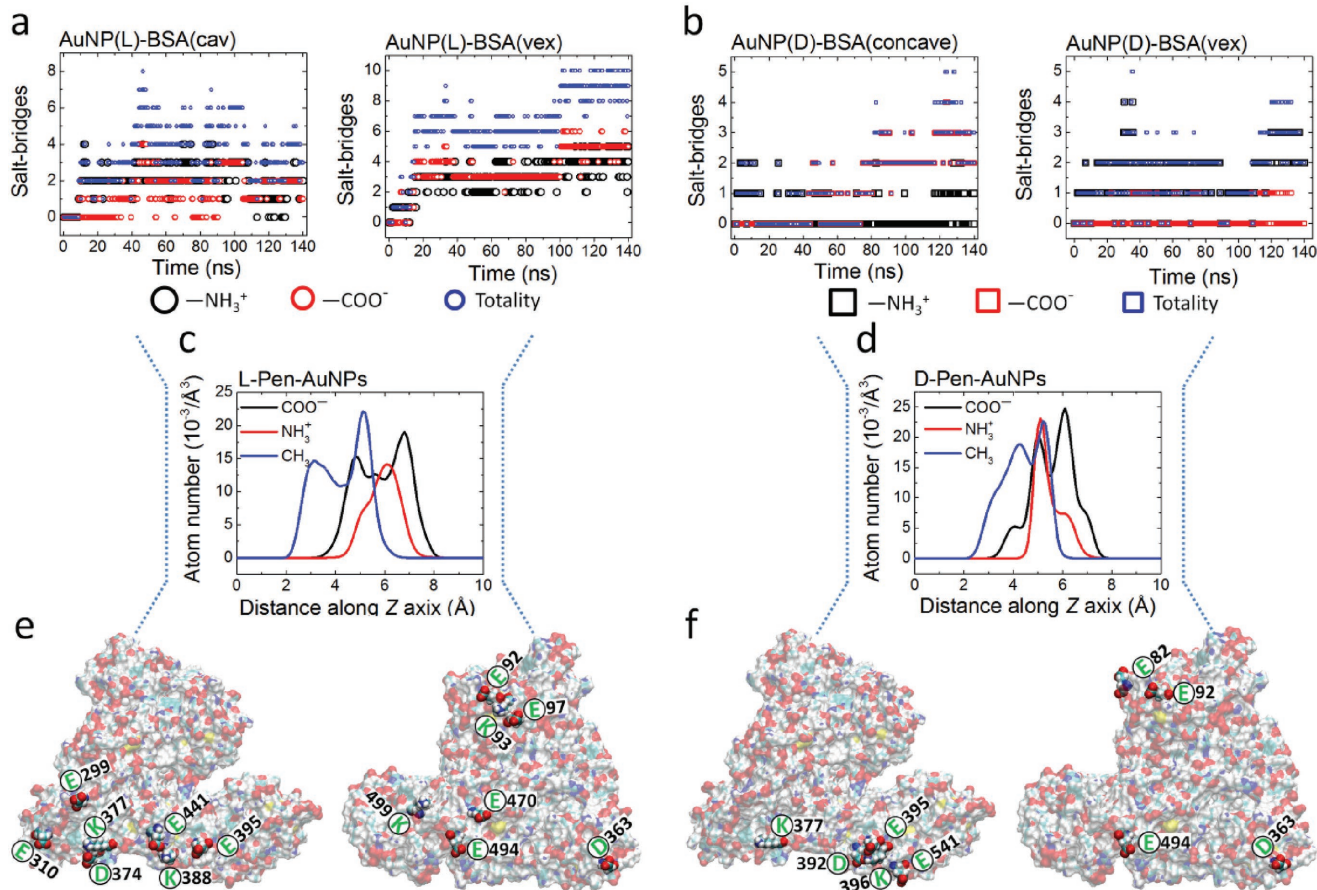
## 2.6. Salt Bridge-Dominant Interaction between BSA and Chiral Surfaces of AuNPs

Table S2 (Supporting Information) lists the amino acids with high contact ratio to chiral surfaces of Pen–AuNPs within 4.5 Å distance. Most of them were charged amino acids, e.g., Glu, Lys, and Asp. Thus, salt bridge interaction plays an important role in dominating the interaction between BSA and chiral surface of Pen–AuNPs. Salt bridges are a combination of hydrogen bonding and electrostatic interactions, which most often arise from the anionic carboxylate ( $\text{RCOO}^-$ ) of either Asp or Glu and the cationic ammonium ( $\text{RNH}_3^+$ ) of Lys or the guanidinium ( $\text{RNHC}(\text{NH}_2)_2^+$ ) of Arg.<sup>[34]</sup> Results (Figure 5a,b) showed that the salt bridge interaction between BSA (concave and convex faces) and the chiral surfaces (L and D) differed in both the

number of salt bridges and the types of amino acids involved. These findings could be associated with the spatial distribution features of functional groups ( $-\text{COO}^-$ ,  $-\text{NH}_3^+$ , and  $-\text{CH}_3$ ) in chiral interfaces (Figure 5c,d). The relative location of carboxyl and amino groups, as well as steric hindrance from methyl groups, might be the key factors to constitute salt bridges with carboxyl and amino groups on the protein surface. In turn, the uneven distribution of charged amino acids on the irregular surface of BSA is also an important factor for salt bridge formation. Further, we marked the amino acids involved in salt bridges in detail on the concave and convex faces of BSA (Figure 5e,f). As an intuitive result, we could understand that the locations and amounts of salt bridges determined the orientation and binding strength of protein on the chiral surfaces of AuNPs.

## 2.7. Influence of Nanochiral Surfaces and Corona Formation on Cell Uptake

Sequentially, we evaluated the uptake of the AuNP–Pen–BSA complex in A549 (human alveolar basal epithelial adenocarcinoma)



**Figure 5.** Formation of salt bridges between BSA and chiral surfaces of Pen-AuNPs. a,b) The number of salt bridges were counted within 4.5 Å distance between the contacted side faces (concave and convex) and L-chiral/D-chiral interfaces. The black cycle/square presents salt bridges formed by  $-\text{NH}_3^+$  groups from amino acid residues of BSA surfaces; the red cycle/square presents salt bridges formed by  $-\text{COO}^-$  groups from amino acid residues of BSA surfaces; and the blue cycle/square presents the total number of salt bridges. c,d) The distribution of  $-\text{COO}^-$  (black),  $-\text{NH}_3^+$  (red), and  $-\text{CH}_3$  (blue) groups on different nanochiral interfaces by counting the amount of each functional group per unit distance (2 Å) along the Z-axis direction based on MD simulation (20 ns). e,f) Localization of representative amino acid residues involves salt bridges on the concave and convex side faces of BSA.

and HaCaT (human keratinocyte) cell lines after 3, 12, and 24 h exposure in serum-free media. The culture medium was supplemented with  $1.5 \times 10^{-6}$  M BSA, which could meet the ratio of NPs to BSA at 1:1000, to consider the effects of the protein corona. AuNP-Pen-BSA uptake was quantified by measuring the amount of Au in cells using the inductively coupled plasma mass spectrometry (ICP-MS) method normalized to the exposure concentration. A significant difference in the internalization of the two chiral AuNP-Pen-BSA mixtures after 3 h of incubation was observed (Figure 6). AuNP(L)-BSA showed significantly higher uptake than AuNP(D)-BSA after 3 h of incubation, which clearly depended on the BSA corona formed on the nanochiral surface. These results could be attributed to BSA adsorption on two kinds of chiral surfaces of Pen-AuNPs with different adsorption orientation, resulting in the exposure of different charged amounts outward. AuNPs(L)-BSA carried more positive charges on the surface of the corona, which easily interact with the negatively charged cell membrane by electrostatic attraction resulting

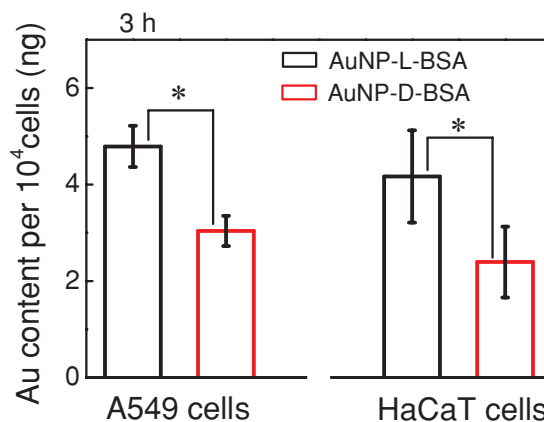


**Figure 6.** Influence of nanochiral surfaces and corona formation on cell uptake. Cell uptakes were normalized to the dose following 3 h exposure to AuNP-Pen-BSA complexes in A549 and HaCaT cells as determined by ICP-MS.



in greater internalization by cells. Differences in cell endocytic efficiency for different nanomaterials are easily detected in the first few hours. These differences then become illegible with the increase in endocytosis time, because the cells tend to show saturated uptake. As shown in Figure S10 of the Supporting Information (12 and 24 h), the differences were gradually decreased due to the saturated cellular uptake.

### 3. Conclusion

We present a systematic investigation of albumin adsorption onto nanoparticles with chiral surfaces. Fluorescent quenching experiments revealed that adsorption of BSA onto both nano-chiral surfaces was a spontaneous and exothermic process. BSA binding to L-chiral surface of AuNPs released more heat and caused a greater  $\Delta S$  change than the D-chiral surface. Protein conformation did not change based on the amide I region ART-IR analysis during adsorption onto Pen-AuNPs. The DLS method used here permitted in situ measurements of hydrodynamic size. Upon BSA binding, Pen-AuNPs showed a radius increase of  $\approx 3$  nm at saturation, indicating the formation of a BSA monolayer on both chiral surfaces of Pen-AuNPs, contacting with their triangular faces. We employed the QCM-D technique to monitor the interaction between BSA-adsorbed Pen-AuNPs and positively charged SLBs, by which we could calculate the locally exposed charges after BSA adsorbed onto chiral surface of AuNPs. A significant difference was observed in that, BSA exposed more negative charges after binding to D-chiral surface than to L-chiral surface, indicating that BSA adsorbed onto two kinds of chiral surfaces with different orientation.

In order to obtain detailed insights, we performed MD simulations to show the details including the number of contacted amino acids, exposed charges, and the height of protein along the interaction time. The results demonstrated that BSA showed different adsorption behaviors on different chiral surfaces, which was in excellent agreement with the experimental data. The salt bridge, as the primary driving force, played key roles in determining BSA adsorption orientation and binding strength onto chiral surfaces. Salt bridge formation was dependent on the spatial distribution features of functional groups ( $-\text{COO}^-$ ,  $-\text{NH}_3^+$ , and  $-\text{CH}_3$ ) of chiral molecules on nanosurfaces and the distribution of charged amino acids on the irregular surface of BSA. Sequentially, BSA corona coated on the nano-chiral surfaces affected the interaction with cells and resulted in different cell uptake between different chiral surfaces. Our study provides a molecular-level understanding of protein corona on nano-chiral surfaces, an important issue in the safety application of chiral nanomaterials.

### 4. Experimental Section

**Materials:** Chloroauric acid ( $\text{HAuCl}_4$ ), trisodium citrate, D-penicillamine, and L-penicillamine were purchased from Alfa Chemical (UK). BSA was obtained from Sigma-Aldrich (Shanghai, China). DOPC and DOEPC lipids were from Avanti Polar Lipids, Inc. (USA). All other chemicals, unless mentioned otherwise, were of reagent grade. Milli-Q grade ( $>18$  M $\Omega$ ) water with ultraviolet sterilization was used throughout the experiments.

**Preparation of AuNPs with Chiral Surfaces:** AuNPs were synthesized by citrate reduction of  $\text{HAuCl}_4$ .<sup>[30]</sup> Briefly, 100 mL of  $\text{HAuCl}_4$  aqueous

solution ( $1 \times 10^{-3}$  M) was brought to a reflux with stirring, and 10 mL of  $38.8 \times 10^{-3}$  M trisodium citrate solution was added. After the color of solution changed from pale yellow to dark red, the reaction mixture was refluxed for another 15 min, and then cooled to room temperature. Subsequently, the prepared AuNPs solution was filtered through a  $0.22 \times 10^{-3}$  M membrane. The molar concentration of AuNPs was about  $15 \times 10^{-9}$  M ( $180 \mu\text{g mL}^{-1}$ ).<sup>[31]</sup>

Modification of AuNPs with chiral Pen was realized by Au-S bonding. Briefly, citrate-protected AuNPs (Cit-AuNPs) were mixed with excess L-Pen or D-Pen, and the mixture was allowed to react overnight at room temperature. After centrifugation ( $13\,000 \times g$  for 30 min), the pellet was resuspended in water and the Pen-modified AuNPs (Pen-AuNPs) were obtained. To obtain the BSA corona around Pen-AuNPs, Pen-AuNPs were incubated with BSA solution (at desired or excess concentration) for not less than 1 h at 37 °C. The superfluous BSA could be discarded by centrifuging at  $13\,000 \times g$  for 30 min, and the pellet was then resuspended in Tris buffer.

The Pen-AuNPs were characterized by TEM analysis using a F20U-TWIN electron microscope (FEI Tecnai) at an accelerating voltage of 200 kV. The characteristic plasmon absorbance band of AuNPs was obtained with a Hitachi U-3010 spectrophotometer (Hitachi, Japan). Hydrodynamic diameter distributions and zeta potential were determined in water using a Zetasizer Nano ZS Malvern (Worcestershire, U.K.) instrument. Attenuated total reflection (ATR)-FTIR spectra were recorded on a Spectrum OneB FTIR Perkin Elmer equipped with a zinc selenide (ZnSe) ATR accessory, and spectra were obtained from a total of 128 scans with a resolution of  $4 \text{ cm}^{-1}$ . CD spectra were measured on a Jasco J-810 spectropolarimeter at room temperature (25 °C) with a 1 mm path quartz cuvette. The CD spectra were recorded from 190–650 nm, and each spectrum was the average of five successive scans.

**Thermodynamic Parameter Measurements by Fluorescence Quenching:** BSA fluorescence quenching induced by Pen-AuNPs was measured on the Enspire Multiskan Ascent plate reader (Perkin Elmer) with an emission wavelength of 330 nm upon 280 nm excitation at two temperatures (300 K, 310 K). The BSA concentration was fixed at  $1.5 \times 10^{-6}$  M, and the concentrations of Pen-AuNPs ranged from 0 to  $15 \times 10^{-9}$  M. Data were analyzed using the Stern Volmer model<sup>[35]</sup>

$$\frac{F_0}{F_0 - F} = \frac{1}{f_a K_a [Q]} + \frac{1}{f_a} \quad (1)$$

where  $F_0$  and  $F$  were the fluorescence intensities of BSA in the absence and presence of quencher (Pen-AuNPs),  $[Q]$  was the concentration of the Pen-AuNPs,  $K_a$  was the effective quenching constant, and  $f_a$  was the mole fraction of free-adsorbed BSA. The corresponding  $K_a$  at different temperatures could be obtained as a quotient of the intercept ( $f_a^{-1}$ ) and slope ( $f_a^{-1} \cdot K_a^{-1}$ ). Sequentially, enthalpy change ( $\Delta H$ ) and entropy change ( $\Delta S$ ) could be calculated according to the van't Hoff equation

$$\ln K_a = -\frac{\Delta H}{RT} + \frac{\Delta S}{R} \quad (2)$$

Gibbs free energy change ( $\Delta G$ ) could be obtained by the following relationship

$$\Delta G = \Delta H - T\Delta S \quad (3)$$

**DLS Measurements:** The hydrodynamic diameters of Pen-AuNPs with the BSA corona were determined by DLS measurement on a Zetasizer Nano ZS Malvern (Worcestershire, UK) at 25 °C. The mixtures of Pen-AuNPs and BSA were incubated for 1 h at 37 °C before DLS measurement. The concentration of Pen-AuNPs was kept at  $5 \times 10^{-9}$  M and BSA solutions with aliquot concentrations were added to obtain the desired Pen-AuNPs:BSA molar ratios ranging from 1:0 to 1:3000. The mean z-average hydrodynamic radius ( $R_H$ ) and the polydispersity index (PI) were obtained based on the cumulants method.<sup>[17b,36]</sup> Here, Pen-AuNPs with BSA corona were considered to be a spherical. So,  $R_H$  and the number of adsorbed BSA ( $N$ ) could be estimated according to the following equation<sup>[18b]</sup>



$$R_H(N) = R_H(0) \sqrt[3]{1 + cN} \quad (4)$$

$R_H(N)$  and  $R_H(0)$  denoted the hydrodynamic radius of Pen–AuNPs with or without BSA corona,  $N$  was the number of adsorbed BSA, the coefficient  $c = V_p/V_0$ .  $V_0$  was the volume of the bare Pen–AuNPs, and  $V_p$  was the molecular volume of BSA. For saturated adsorption, the hydrodynamic radius could be expressed as in the following equation

$$R_H(N_{\max}) = R_H(0) + \Delta R = R_H(0) \sqrt[3]{1 + cN_{\max}} \quad (5)$$

$N_{\max}$  was the maximum number of protein molecules adsorbed onto the Pen–AuNPs. The relationship of  $N$  and protein concentration [protein] (free protein in the solution) could be described by the Hill equation

$$N = N_{\max} \frac{1}{1 + (K_D/[BSA])^n} \quad (6)$$

In our experiment, the measurements were performed three times, and data were fitted using Hill equation to obtain the dissociation constant ( $K_D$ ), Hill coefficient ( $n$ ), protein layer thickness ( $\Delta R_H$ ), and  $N_{\max}$  values.

**Synchrotron Radiation ATR-FTIR Measurements:** ATR-FTIR spectra were recorded on a Nicolet 6700 from BL01B beamline of National Facility for Protein Science Shanghai (NFPS) at Shanghai Synchrotron Radiation Facility. After the mixtures of Pen–AuNPs and BSA at a molar ratio of 1:500 were incubated for 1 h, the concentrate of sample drop was cast onto the sample holder. Spectra were recorded between 4000 and 400  $\text{cm}^{-1}$  after a fully dried sample film formed on the sample holder. Secondary structures of BSA were assessed by the SD and FSD in the spectral region of amide I (1600–1700  $\text{cm}^{-1}$ ).<sup>[24,37]</sup> Assignment of amide I band frequencies to secondary structures of protein are shown in Table S1 (Supporting Information).

**QCM-D Measurements:** Positively charged SLBs comprising DOPC and DOEPC (8:2) were constructed by surface-mediated vesicle fusion,<sup>[38]</sup> supported on silicon dioxide coated piezoelectric crystals (Q-Sense QSX 303, 50 nm) in a QCM-D equipment (Q-Sense E4, Sweden). The prepared bilayers were washed with 2-[4-(2-hydroxyethyl)-1-piperazinyl]ethanesulfonic acid buffer ( $10 \times 10^{-3}$  M, pH 7.4, without salt) at a flow rate of 150  $\mu\text{L min}^{-1}$  until the frequency and dissipation values reached stabilization. The BSA-adsorbed Pen–AuNP (AuNP–Pen–BSA) solution was then injected at a flow rate of 20  $\mu\text{L min}^{-1}$  till the signals tended to the stabilization. The frequency change ( $\Delta f$ ) was used to scale the mass of NPs adsorbed onto the SLBs.

**ICP-MS Detection of Cellular Uptake:** Cellular uptake of AuPNs coated with BSA corona was determined by ICP-MS (NexION 300X, PerkinElmer, USA). A549 and HaCaT cells were seeded in 6-well microplates, supplemented with 10% fetal bovine serum (FBS) and 1% penicillin-streptomycin, and maintained in a humidified atmosphere containing 5%  $\text{CO}_2$  at 37 °C. When cells reached 90% confluence, the media were removed and each well was carefully washed three times with phosphate buffer saline (PBS). The cells were then incubated with 15  $\mu\text{g mL}^{-1}$  of AuNP–BSA–corona mixtures dispersed in 1640 or Dulbecco's modified Eagle medium without FBS at 37 °C for 3 h. Sequentially, the cells were washed thrice with PBS, trypsinized, counted, and centrifuged to obtain the precipitates. The cell pellets were then digested overnight using nitric acid (Optima grade, 70%), evaporated, and treated with aqua regia to dissolve the AuNPs until the solutions became transparent. Finally, the solutions were diluted to certain volume and analyzed by ICP-MS to measure the Au amount per cell. The data are presented as the mean  $\pm$  S.D. of three independent measurements.

**MD Simulations:** In MD simulation, we did not build a full-size AuNP ( $\approx 14$  nm) system but focused on the contact interface between the protein and Pen–AuNPs, which was considered as a plane surface. The chiral Pen molecules bound to the Au atom by an Au–S bond are shown in a 6d pattern (Figure S9, Supporting Information). In the simulation box, the Pen monolayer laid along XY plane with a size of  $115 \times 119 \text{ \AA}^2$ , which was sufficient to accommodate the adsorbed

protein. Four systems were to be built involving two kinds of chiral interfaces (L-Pen and D-Pen) and two triangular sides of BSA (concave and convex) in our MD simulation. The horizontal dimension of the simulation box was the same as the chiral interface ( $115 \times 119 \text{ \AA}^2$ ) and the height was 129  $\text{\AA}$ . There were about 49 000 water molecules in each simulation system and up to 170 000 atoms in total.

The simulations were performed using Gromacs 5 program. CHARMM36 all-atom force field was used to describe the protein BSA. The force field for assembling the molecules was generated by CGENFF.<sup>[39]</sup> The water model was TIP3P. Van der Waals interactions were treated by the switch function with twin-range cutoff distances of 10 and 12  $\text{\AA}$ , and electrostatic interactions were calculated by the particle mesh Ewald method with a cutoff distance of 12  $\text{\AA}$ . Periodic boundary conditions were applied in all three coordinate directions. In all cases, dynamics were sampled from the canonical constant temperature, constant volume ensemble ( $T = 300$  K), and the Langevin thermostat method was used with a damping coefficient of 1  $\text{ps}^{-1}$ . All snapshots were rendered with VMD software.

**Statistical Analysis:** Results are expressed as mean  $\pm$  standard deviation and all values were obtained from at least three independent experiments. Statistical significance was evaluated using one-way analysis of variance (ANOVA) and Student's *t*-test. Statistical differences were considered significant for  $p < 0.05$ .

## Supporting Information

Supporting Information is available from the Wiley Online Library or from the author.

## Acknowledgements

X.W. and X.W. contributed equally to this work. This work was financially supported by the National Natural Science Foundation of China (NSFC) (Grant Nos. 21320102003, 11435002, and 31571025), the National Basic Research Program of China (Grant No. 2016YFA0201600), the Science Fund for Creative Research Groups of the National Natural Science Foundation of China (Grant No. 11621505), CAS Key Research Program of Frontier Sciences (Grant No. QYZDJ-SSW-SLH022), and the NSFC Distinguished Young Scholars (Grant No. 11425520).

## Conflict of Interest

The authors declare no conflict of interest.

## Keywords

chiral surfaces, molecular dynamic simulation, nanoparticles, protein adsorption behavior

Received: November 14, 2017

Revised: February 5, 2018

Published online:

[1] a) W. Ma, L. Xu, A. F. de Moura, X. Wu, H. Kuang, C. Xu, N. A. Kotov, *Chem. Rev.* **2017**, *117*, 8041; b) Y. Wang, J. Xu, Y. Wang, H. Chen, *Chem. Soc. Rev.* **2013**, *42*, 2930.

[2] a) A. Kuzyk, R. Schreiber, Z. Fan, G. Pardatscher, E.-M. Roller, A. Hoegle, F. C. Simmel, A. O. Govorov, T. Liedl, *Nature* **2012**, *483*,

- 311; b) J. Lv, K. Hou, D. Ding, D. Wang, B. Han, X. Gao, M. Zhao, L. Shi, J. Guo, Y. Zheng, X. Zhang, C. Lu, L. Huang, W. Huang, Z. Tang, *Angew. Chem., Int. Ed.* **2017**, *56*, 5055.
- [3] a) H. Zhao, K. Min, N. R. Aluru, *Nano Lett.* **2009**, *9*, 3012; b) R. F. Zhang, Y. Y. Zhang, F. Wei, *Acc. Chem. Res.* **2017**, *50*, 179.
- [4] a) E. Gross, J. H. Liu, S. Alayoglu, M. A. Marcus, S. C. Fakra, F. D. Toste, G. A. Somorjai, *J. Am. Chem. Soc.* **2013**, *135*, 3881; b) M. Kaushik, K. Basu, C. Benoit, C. M. Cirtiu, H. Vali, A. Moores, *J. Am. Chem. Soc.* **2015**, *137*, 6124.
- [5] a) E. Hendry, T. Carpy, J. Johnston, M. Popland, R. V. Mikhaylovskiy, A. J. Laphorn, S. M. Kelly, L. D. Barron, N. Gadegaard, M. Kadodwala, *Nat. Nanotechnol.* **2010**, *5*, 783; b) S. Jahani, Z. Jacob, *Nat. Nanotechnol.* **2016**, *11*, 23.
- [6] a) N. Bertrand, J. Wu, X. Xu, N. Kamaly, O. C. Farokhzad, *Adv. Drug Delivery Rev.* **2014**, *66*, 2; b) S. J. Klaine, P. J. J. Alvarez, G. E. Batley, T. F. Fernandes, R. D. Handy, D. Y. Lyon, S. Mahendra, M. J. McLaughlin, J. R. Lead, *Environ. Toxicol. Chem.* **2008**, *27*, 1825.
- [7] a) Y. Li, Y. Zhou, H.-Y. Wang, S. Perrett, Y. Zhao, Z. Tang, G. Nie, *Angew. Chem., Int. Ed.* **2011**, *50*, 5860; b) F. Gao, M. Sun, W. Ma, X. Wu, L. Liu, H. Kuang, C. Xu, *Adv. Mater.* **2017**, *29*, 1606864.
- [8] a) E. Casals, T. Pfaller, A. Duschl, G. J. Oostingh, V. Puentes, *ACS Nano* **2010**, *4*, 3623; b) S. Tenzer, D. Docter, J. Kuharev, A. Musyanovych, V. Fetz, R. Hecht, F. Schlenk, D. Fischer, K. Kiouptsi, C. Reinhardt, K. Landfester, H. Schild, M. Maskos, S. K. Knauer, R. H. Stauber, *Nat. Nanotechnol.* **2013**, *8*, 772.
- [9] A. E. Nel, L. Madler, D. Velegol, T. Xia, E. M. V. Hoek, P. Somasundaran, F. Klaessig, V. Castranova, M. Thompson, *Nat. Mater.* **2009**, *8*, 543.
- [10] M. Zhang, G. Qing, T. Sun, *Chem. Soc. Rev.* **2012**, *41*, 1972.
- [11] a) G. Qing, S. Zhao, Y. Xiong, Z. Lv, F. Jiang, Y. Liu, H. Chen, M. Zhang, T. Sun, *J. Am. Chem. Soc.* **2014**, *136*, 10736; b) G. Gao, M. Zhang, P. Lu, G. Guo, D. Wang, T. Sun, *Angew. Chem., Int. Ed. Engl.* **2015**, *54*, 2245.
- [12] a) X. Zhao, L. Xu, M. Sun, W. Ma, X. Wu, C. Xu, H. Kuang, *Nat. Commun.* **2007**, *8*, 1; b) A. Motealleh, N. Seda Kehr, *ACS Appl. Mater. Interfaces* **2017**, *9*, 33674; c) N. S. Kehr, J. Jose, *Appl. Surf. Sci.* **2017**, *425*, 432; d) N. S. Kehr, *Biomacromolecules* **2016**, *17*, 1117; e) J. El-Gindi, K. Benson, L. De Cola, H. J. Galla, N. S. Kehr, *Angew. Chem., Int. Ed. Engl.* **2012**, *51*, 3716; f) J. Deng, S. Wu, M. Yao, C. Gao, *Sci. Rep.* **2016**, *6*, 1.
- [13] a) X. Wang, M. Wang, R. Lei, S. F. Zhu, Y. Zhao, C. Chen, *ACS Nano* **2017**, *11*, 4606; b) K. Lv, L. Zhang, W. S. Lu, M. H. Liu, *ACS Appl. Mater. Interfaces* **2014**, *6*, 18878.
- [14] M. Mahmoudi, I. Lynch, M. R. Ejtehadi, M. P. Monopoli, F. B. Bombelli, S. Laurent, *Chem. Rev.* **2011**, *111*, 5610.
- [15] a) O. Lopez-Acevedo, H. Tsunoyama, T. Tsukuda, H. Hakkinen, C. M. Aikens, *J. Am. Chem. Soc.* **2010**, *132*, 8210; b) A. Ben-Moshe, S. G. Wolf, M. Bar Sadan, L. Houben, Z. Fan, A. O. Govorov, G. Markovich, *Nat. Commun.* **2014**, *5*, 1.
- [16] a) X. Lan, Q. Wang, *Adv. Mater.* **2016**, *28*, 10499; b) X. Wang, Z. Tang, *Small* **2017**, *13*, 1.
- [17] a) S. H. D. P. Lacerda, J. J. Park, C. Meuse, D. Pristiniski, M. L. Becker, A. Karim, J. F. Douglas, *ACS Nano* **2010**, *4*, 365; b) D.-H. Tsai, F. W. DelRio, A. M. Keene, K. M. Tyner, R. I. MacCuspie, T. J. Cho, M. R. Zachariah, V. A. Hackley, *Langmuir* **2011**, *27*, 2464.
- [18] a) Z. Zeng, X. Shi, T. Mabe, S. Christie, G. Gilmore, A. W. Smith, J. Wei, *Anal. Chem.* **2017**, *89*, 5221; b) C. Roecker, M. Poetzl, F. Zhang, W. J. Parak, G. U. Nienhaus, *Nat. Nanotechnol.* **2009**, *4*, 577.
- [19] a) F. Spinozzi, G. Cecccone, P. Moretti, G. Campanella, C. Ferrero, S. Combet, I. Ojeajimenez, P. Ghigna, *Langmuir* **2017**, *33*, 2248; b) J. Wang, U. B. Jensen, G. V. Jensen, S. Shipovskov, V. S. Balakrishnan, D. Otzen, J. S. Pedersen, F. Besenbacher, D. S. Sutherland, *Nano Lett.* **2011**, *11*, 4985.
- [20] a) A. E. Frise, E. Edri, I. Furo, O. Regev, *J. Phys. Chem. Lett.* **2010**, *1*, 1414; b) M. Kokkinopoulou, J. Simon, K. Landfester, V. Mailaender, I. Lieberwirth, *Nanoscale* **2017**, *9*, 8858.
- [21] a) C. Ge, J. Du, L. Zhao, L. Wang, Y. Liu, D. Li, Y. Yang, R. Zhou, Y. Zhao, Z. Chai, C. Chen, *Proc. Natl. Acad. Sci. USA* **2011**, *108*, 16968; b) A. Karner, B. Nimmervoll, B. Plochberger, E. Klotzsch, A. Horner, D. G. Knyazev, R. Kuttner, K. Winkler, L. Winter, C. Siligan, N. Ollinger, P. Pohl, J. Preiner, *Nat. Nanotechnol.* **2017**, *12*, 260.
- [22] a) T. Cedervall, I. Lynch, S. Lindman, T. Berggard, E. Thulin, H. Nilsson, K. A. Dawson, S. Linse, *Proc. Natl. Acad. Sci. USA* **2007**, *104*, 2050; b) X. Zhang, J. Zhang, F. Zhang, S. Yu, *Nanoscale* **2017**, *9*, 4787.
- [23] a) H. Shinmori, C. Mochizuki, *Chem. Commun.* **2017**, *53*, 6569; b) S. Laera, G. Cecccone, F. Rossi, D. Gilliland, R. Hussain, G. Siligardi, L. Calzolari, *Nano Lett.* **2011**, *11*, 4480.
- [24] a) H. Yang, S. Yang, J. Kong, A. Dong, S. Yu, *Nat. Protoc.* **2015**, *10*, 382; b) M. Wang, C. Fu, X. Liu, Z. Lin, N. Yang, S. Yu, *Nanoscale* **2015**, *7*, 15191.
- [25] a) Q. Hu, X. Bai, G. Hu, Y. Y. Zuo, *ACS Nano* **2017**, *11*, 6832; b) A. P. S. Brogan, R. B. Sessions, A. W. Perriman, S. Mann, *J. Am. Chem. Soc.* **2014**, *136*, 16824.
- [26] A. Bujacz, *Acta Crystallogr., Sect. D: Biol. Crystallogr.* **2012**, *68*, 1278.
- [27] A. O. Elzoghby, W. M. Samy, N. A. Elgindy, *J. Controlled Release* **2012**, *157*, 168.
- [28] a) E. C. Dreaden, A. M. Alkilany, X. H. Huang, C. J. Murphy, M. A. El-Sayed, *Chem. Soc. Rev.* **2012**, *41*, 2740; b) E. Boisselier, D. Astruc, *Chem. Soc. Rev.* **2009**, *38*, 1759.
- [29] a) A. Guerrero-Martinez, J. Lorenzo Alonso-Gomez, B. Auguie, M. Magdalena Cid, L. M. Liz-Marzan, *Nano Today* **2011**, *6*, 381; b) A. Ben-Moshe, B. M. Maoz, A. O. Govorov, G. Markovich, *Chem. Soc. Rev.* **2013**, *42*, 7028.
- [30] J. Liu, Y. Lu, *Nat. Protoc.* **2006**, *1*, 246.
- [31] X. H. N. Xu, S. Huang, W. Brownlow, K. Salaita, R. B. Jeffers, *J. Phys. Chem. B* **2004**, *108*, 15543.
- [32] D. J. Maxwell, J. R. Taylor, S. M. Nie, *J. Am. Chem. Soc.* **2002**, *124*, 9606.
- [33] a) B. H. J. Gottschalck, *J. Chem. Phys.* **2002**, *116*, 784; b) Y. X. Younan Xia, B. Lim, S. E. Skrabalak, *Angew. Chem., Int. Ed. Engl.* **2009**, *48*, 60; c) T. P. Martin, *Phys. Rep.* **1996**, *273*, 199.
- [34] C. D. Waldburger, J. F. Schildbach, R. T. Sauer, *Nat. Struct. Biol.* **1995**, *2*, 122.
- [35] L. Shang, Y. Wang, J. Jiang, S. Dong, *Langmuir* **2007**, *23*, 2714.
- [36] M. Cui, R. Liu, Z. Deng, G. Ge, Y. Liu, L. Xie, *Nano Res.* **2014**, *7*, 345.
- [37] a) A. Dong, P. Huang, W. S. Caughey, *Biochemistry* **1990**, *29*, 3303; b) P. Roach, D. Farrar, C. C. Perry, *J. Am. Chem. Soc.* **2006**, *128*, 3939.
- [38] N. J. Cho, C. W. Frank, B. Kasemo, F. Hook, *Nat. Protoc.* **2010**, *5*, 1096.
- [39] K. Vanommeslaeghe, E. Hatcher, C. Acharya, S. Kundu, S. Zhong, J. Shim, E. Darian, O. Guvench, P. Lopes, I. Vorobyov, A. D. MacKerell Jr., *J. Comput. Chem.* **2010**, *31*, 671.